IL NUOVO CIMENTO **44 C** (2021) 6
DOI 10.1393/ncc/i2021-21006-9

COMMUNICATIONS: SIF Congress 2020

Pixel chamber: A solid-state bubble chamber for imaging of charm and beauty

A. MULLIRI([2]) on behalf of M. ARBA([1]), P. BHATTACHARYA([2]), E. CASULA([2]), C. CICALÒ([1]), A. DE FALCO([2]), D. MARRAS([1]), A. MASONI([1]), S. SIDDHANTA([1]), M. TUVERI([1]) and G. USAI([2])

([1]) *INFN, Sezione di Cagliari - Cagliari, Italy*
([2]) *Dipartimento di Fisica, Università di Cagliari - Cagliari, Italy*

received 4 February 2021

Summary. — The Pixel Chamber project proposes to realize the first "solid-state bubble chamber" detector for measurements of charm and beauty. It is conceived as a stack of hundreds of thin and granular monolithic pixel sensors which provide a 3D image of all of the particles produced in proton-silicon interactions occurring inside the detector volume. In this paper we will discuss the high-precision tracking and vertexing performances, showing that the vertex resolution can be up to one order of magnitude better than state-of-the-art detectors like the LHCb one.

1. – Introduction

The heart of modern vertex detectors are silicon trackers consisting of cylindrical or planar layers of silicon sensors, generally immersed in a magnetic field. For example, the new ALICE Inner Tracking System at the CERN LHC consists of 7 cylinders of monolithic silicon pixel active sensors (MAPS) [1, 2], with the first layer at ~ 2 cm from the interaction point. This detector is used for precision measurements of the particles produced in the interactions and, in particular, of the decay products of particles with long mean life, such as open charm and beauty [1, 2].

With this type of detectors the vertices are calculated by extrapolating tracks reconstructed from hits in the tracking layers. It is therefore important to have a very good spatial resolution and to be very close to the interaction point.

In this sense, bubble chambers were attractive trackers since they acted as a target and had a good spatial resolution (~ 10 μm). However, these detectors have a low time resolution ($\sim$ ms) which does not make them suitable for modern experiments in which the event rate can be much larger, in order to study rare processes like charm or beauty production.

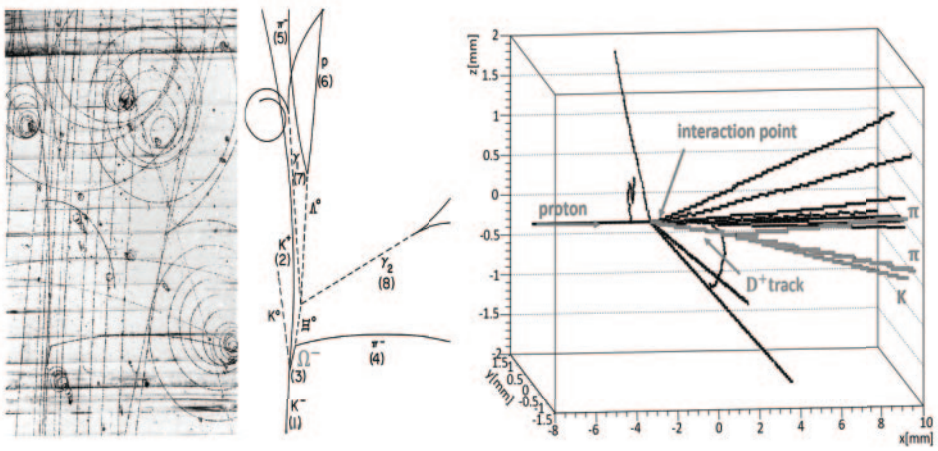

Fig. 1. – Left: image of the Ω discover with a bubble chamber [5]. Right: Geant4 simulation of p-Si interaction with the production of a D^+ meson inside Pixel Chamber.

A silicon-based modern detector, which acts as an active-target capable to image particles in 3D, similarly to a bubble chamber, does not exist. Ideas for a silicon active-target providing continuous tracking were put forward already almost 40 years ago [3], but the required technology just did not exist until recently.

In this paper we describe a proposal for building the first silicon active-target based on silicon pixel sensors, called Pixel Chamber [4], capable to perform continuous, high-resolution ($\sim \mu$m) 3D tracking, including open charm and beauty particles. The aim is to create a bubble chamber-like high-granularity stack of hundreds of very thin monolithic active pixel sensors (MAPS). In fig. 1 a comparison is shown between a bubble chamber image with a strange baryon Ω^- [5] and an image of a Geant4 simulation [6] of a D^+ meson decaying to $K\pi\pi$ in a proton-silicon interaction with Pixel Chamber.

The paper describes the concept of the detector in terms of existing MAPS. We focus then on the detector capabilities in terms of tracking and vertex reconstruction.

2. – Pixel Chamber: geometry and technology

In particle physics experiments, standard hybrid sensor technology dominated the past 20 years. Hybrid detectors have a fast temporal response (the Giga Tracker of NA62 provides single-hit timing with 200 ps RMS resolution [7]) and are radiation hard (10^{16} equivalent neutrons (n_{eq}) per cm^2 for the new sensors designed for HL-LHC [8]). However, the silicon sensor is bump-bonded on the readout chip with a total thickness of hundreds of μm. In addition, in state-of-the-art sensors the pixel pitch is limited to ~ 50 μm.

In monolithic sensors the front-end electronics is integrated in the pixel cell. Such sensors have a thickness reduced to tens of microns and the spatial resolution reaches few μm. Since there is no need to couple two silicon chips, monolithic sensors have a significantly lower production cost.

A monolithic pixel cell contains a charge collection zone deposited on a silicon substrate in a commercial CMOS technology. For Pixel Chamber we explore the possibility

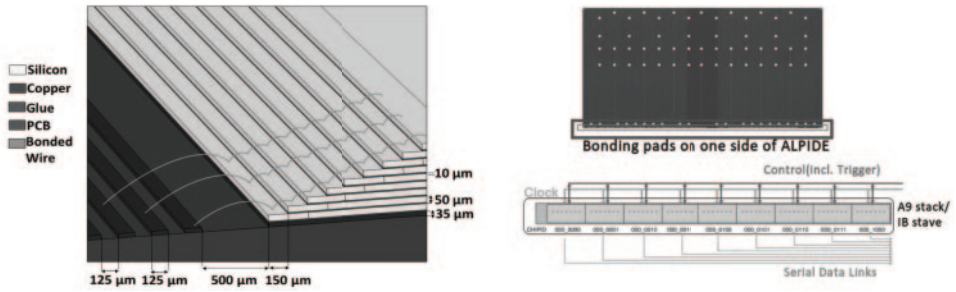

Fig. 2. – Left: the A9 stack scheme showing the wire bonding of the staggered sensors on a PCB. Right-top: bonding pads on ALPIDE. Right-bottom: clock, control and data signals from the A9 stack (the same as the ALICE ITS Inner Barrel stave [10]).

to use the high-performance ALPIDE MAPS sensor recently developed for the ALICE vertex detector [9].

This sensor chip is produced in the TowerJazz 180 nm CMOS imaging process and contains a matrix of 1024×512 pixels [2] (pixel size $\sim 29 \times 27 \mu m^2$), with a thickness of just 50 μm. The pixel contains a deep p-well which prevents PMOS transistors from collecting charge. This allows complex in-pixel amplification, shaping, discrimination and buffering to be implemented within the pixel. The sensor is designed to work at 50 kHz interaction rate with Pb beams and several hundreds kHz interaction rate with proton beams (LHC running conditions). It features a moderate radiation hardness, at the level of fluences of 10^{13} n_{eq}/cm^2 and very low power consumption (~ 40 mW/cm^2).

The proposed basic unit of Pixel Chamber is a stack of nine ALPIDE sensors —called the A9 stack. The scheme is shown in fig. 2, left. The nine sensors are arranged in a staggered fashion to provide the space for wire bonding of the sensor pads. The pads, which provide access to the signal and power circuits of the sensor, reside on one side of the surface of the sensor along its length (fig. 2, right-top). The offset between sensor layers is 150 μm. Between two sensors there will be a layer of electrically insulating glue with a thickness of about 10 μm. The total thickness of the A9 stack is 530 μm. The 9 ALPIDE sensors in the A9 stack have individual 1.2 Gbps serial data lines, a shared bi-directional differential control and monitoring line and a shared differential clock line (fig. 2, right-bottom). The data, control, monitoring and clock signals are interfaced on a PCB through wire bonds.

Pixel Chamber is an assembly of 24 A9 stacks —for a total of 216 sensors— that form the full stack (thickness: 13 mm) along the scheme shown in fig. 3, left. The width of the usable active area is 10 mm making the chamber active volume to be $30 \times 13 \times 10$ mm^3. In Pixel Chamber, signal and power lines will be distributed by a combination of rigid and flex PCBs. The rigid part will host the wire bonds and will extend 1.2 mm inwards from the periphery of the first sensor of the A9 stack (see fig. 3, left). The flex PCBs is a continuation of the rigid PCBs and will be connected to a patch-panel interfaced to the Readout Units, as shown in fig. 3, right.

3. – Simulation studies

The detector performance was studied with Geant4 (G4) [6], which is used to implement the geometry of the stack of 216 ALPIDE chips and to simulate proton-silicon

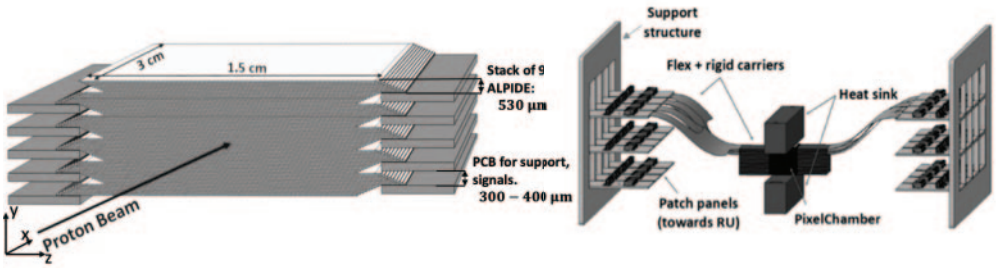

Fig. 3. – Left: view of the Pixel Chamber stack. Right: Pixel Chamber integrated with flexible and rigid PCBs connected to patch-panels for interfacing with the readout system of ALICE ITS.

interactions. The reference system is shown in fig. 3, left: the x-axis defines the beam direction (fig. 1, right), while the y-axis is directed vertically along the stack. The pixel pitch is ~ 30 μm along the x and z axes and 50 μm along the y-axis (the sensor thickness).

A beam of 400 GeV protons is sent towards the detector front-side to generate p-Si inelastic interactions. Charm production in p-Si was also simulated considering, for instance, D^0 or $D^{\pm}$ particles. Since G4 does not generate charmed particles in proton interactions, it is necessary to perform a separate simulation in which D^0 particles (or other charmed particles) are generated in the p-Si interaction point according to the kinematics parameters (rapidity and transverse momentum) evaluated with POWHEG [11]. G4 takes care of the tracking and decaying of the charmed particles and of the tracking of the products.

In this first study, the charge spread across different pixels is not considered so that the pixel cluster size is one.

From the G4 simulation, a dataset is obtained for particles produced in p-Si interactions, including D^0 decay products. The dataset contains various information including the coordinates of the center of the pixels crossed by a particle (hits) and useful information for the Monte Carlo (MC) truth, such as momentum, energy, PDG code and production vertex of the particles that generate a hit in the detector.

4. – Track reconstruction

A track reconstruction algorithm based on hit density was developed and tested with the G4 simulation. It is divided in several steps.

First, the search of hit pixels neighbours is performed. The pixels coordinates are defined in terms of integer indices i, j, k. For a given hit pixel, a hit pixel neighbour is another hit pixel at a distance of 1 (fig. 4). The computational time for the neighbours search on n pixels is $O(n^2)$. To optimize it, hit pixels are first ordered by increasing x (index i) coordinates using the recursive sorting algorithm called quicksorting [12], which takes about $n \cdot \log(n)$ cycles to sort n items.

If a pixel has more than a certain number of neighbours N_{neigh}, it is added to a cluster. This density-based grouping is qualitatively similar to DBSCAN [13]. However, in this way tracks that originate from a common point (vertex) would be merged. To solve this problem, an upper limit on the number of neighbours is also applied to split tracks in regions with high hit density. For this reason, a hit is added to a cluster if $1 < N_{\text{neigh}} < 4$ (fig. 4), otherwise it is considered as a noise point.

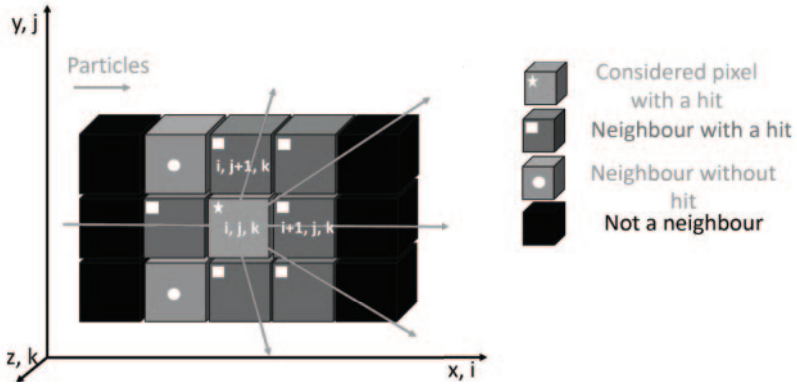

Fig. 4. – Illustration of pixels neighbours with index coordinates.

After this step, most of the tracks are still split in small clusters. The second step is a fit of all found clusters with a linear track model and the obtained fit parameters are then used to further merge clusters belonging to the same track. In the fit, we take as coordinate errors the expected standard deviation for a position measurement with a digital pixel of given pitch. The vector of parameters obtained from the track fit contains the y, z coordinates of a reference point along the line and the y, z direction cosines normalized to the x-direction cosine (α, β). The fit of a track with N points has $2N - 4$ degrees of freedom.

Two fitted clusters are merged together if they have compatible direction cosines, if their extreme points are closer than 70 μm and if the reduced χ^2 (χ^2/ndf) of the track fit is smaller than 1.5. With this first merge, many short clusters are merged to form longer tracks.

At this stage, many noise points can still be present. For this reason, the next step is to attempt to group these points. The clustering algorithm on noise points is repeated twice with less stringent conditions on the number of neighbours, *i.e.*, $1 < N_{\text{neigh}} < 5$ and $1 < N_{\text{neigh}} < 7$.

The merge procedure is then repeated on all clusters until no clusters can be merged any more. Finally, the reconstruction algorithm tries to join residual noise points to tracks that are at a distance of less than 40 μm and performs a cluster merge with a less stringent condition on the χ^2/ndf of the resulting track (χ^2/ndf < 2.5).

In this way, most of the rectilinear tracks are well reconstructed, while non-rectilinear tracks are still broken, as shown in fig. 5. Non-rectilinear tracks are mostly due to low energy particles, such as δ electrons, and therefore of little interest. Some tracks collinear to the incoming proton are still broken. Indeed, at very forward rapidity, tracks are very close to each other and the density of points in such regions is so high that it is difficult to perform a good reconstruction.

The track reconstruction efficiency is calculated as the ratio of the MC hadronic tracks that produce more than 50 hits in the detector and the number of reconstructed tracks compatible with them. A reconstructed track is considered as compatible with a MC track, if they overlap with the requirement that they have compatibles direction cosines and the smallest distance between the extreme points of the reconstructed and MC tracks is less than 70 μm.

The track reconstruction efficiency is almost 80% considering all interactions, and grows up to almost 90% applying a cut to exclude events where the impinging proton

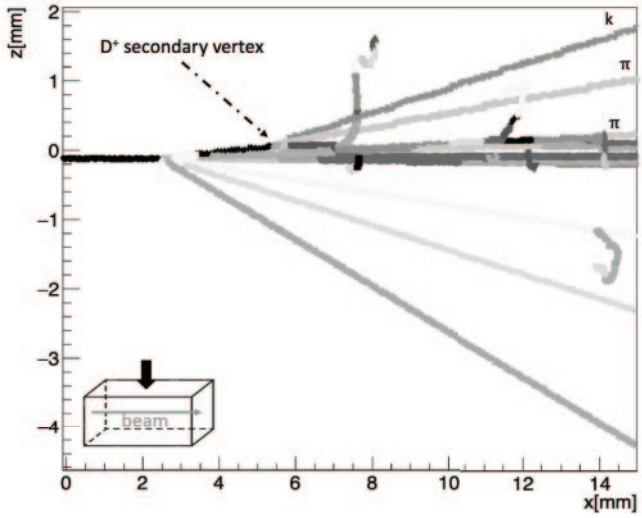

Fig. 5. – Display of the reconstructed tracks of one event with a proton-silicon inelastic interaction and D^+ decay products tracks.

interacts close to the detector end (last 10 mm, fig. 6). The reason of this decrease is that when the proton interacts close to the end of the detector, hadronic tracks are progressively shorter and more difficult to resolve.

5. – Reconstruction of the interaction point (primary vertex)

The algorithm for vertex reconstruction is based on a method used in several other experiments, such as LHCb and ALICE [14] and earlier, CERES and NA60 [15].

The aim is to determine the x_v, y_v, z_v vertex coordinates, while the tracks are not refitted.

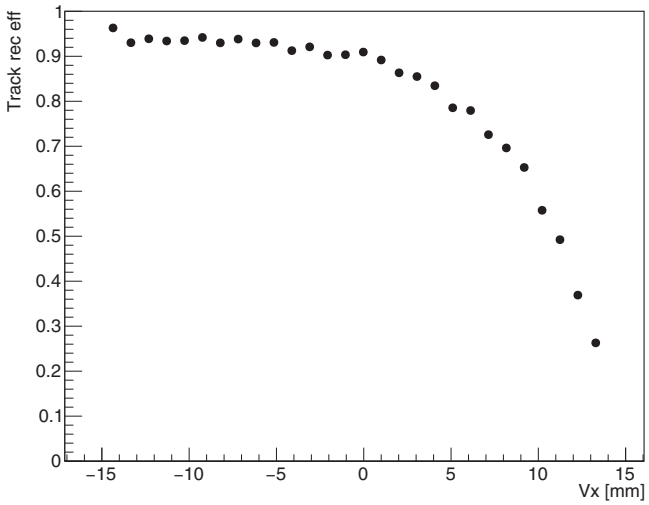

Fig. 6. – Average track reconstruction efficiency, as a function of the interaction point.

We define the vector of the y_v, z_v coordinates:

$$h_i = \begin{pmatrix} y_v \\ z_v \end{pmatrix}. \tag{1}$$

The initial values of x_v, y_v, z_v are set as the coordinates of the last point of proton track which is reasonably close to the interaction point. The proton track is identified as the one that begins at the entrance to the detector.

For each reconstructed track with more than 50 points and $\chi^2/\mathrm{ndf} < 2.5$, one calculates the vector of y, z coordinates corresponding to x_v based on the fitted parameters:

$$q_i = \begin{pmatrix} y_{0i} - (x_v - x_{0i})\alpha_i \\ z_{0i} - (x_v - x_{0i})\beta_i \end{pmatrix}. \tag{2}$$

Using h_i, q_i, the impact parameter χ^2_{IP} is evaluated:

$$\chi^2_{\mathrm{IP}i} = (q_i - h_i)^T V_i^{-1} (q_i - h_i), \tag{3}$$

where V_i is the track covariance matrix obtained from the track fit.

A weight W_{T} is assigned to each track on the basis of its χ^2_{IP}. The weight depends on the ratio between the χ^2_{IP} and the so-called Tukey constants C_{T}:

$$\begin{aligned} W_{\mathrm{T}i} &= \left(1 - \frac{\chi^2_{\mathrm{IP}i}}{C^2_{\mathrm{T}}}\right), && \text{if } \chi^2_{\mathrm{IP}i} < C_{\mathrm{T}}, \\ W_{\mathrm{T}i} &= 0, && \text{if } \chi^2_{\mathrm{IP}i} > C_{\mathrm{T}}. \end{aligned} \tag{4}$$

This allows to avoid to associate to the primary vertex tracks than could worsen the vertex estimation.

The primary vertex χ^2_{PV} is obtained summing each track χ^2_{IP} weighted by W_{T}, and it is then minimized to obtain the vertex coordinates:

$$\chi^2_{\mathrm{PV}} = \sum_{i=1}^{n_{\mathrm{tracks}}} \chi^2_{\mathrm{IP}i} W_{\mathrm{T}i}. \tag{5}$$

The procedure is iterative and the χ^2_{PV} is recalculated at each iteration for decreasing values of C_{T}. The initial value of C_{T} is set to 10^6 to avoid convergence in a local minimum. At each iteration, the vector h_i is updated and the values of χ^2_{IP} and W_{T} are recalculated. In this way, the tracks that in a specific iteration had a weight equal to zero are retested and if their weight is different from zero they contribute to the fit. The iteration is stopped when χ^2_{PV} has converged to a stable value.

Figure 7 shows the distribution of the $\chi^2_{\mathrm{PV}}/\mathrm{ndf}$. There is a peak at zero due to primary vertices with only one or two tracks. If the track multiplicity is 1 the interaction occurs at the end of the detector and no track except the proton verifies the conditions necessary to be associated with the vertex.

If we consider reconstructed vertices with $\chi^2_{\mathrm{PV}}/\mathrm{ndf} < 2.5$ and track multiplicity bigger than 2, the efficiency of the vertex reconstruction is 93%. Removing interactions occurred in the last 10 mm of the detector, the reconstruction efficiency reaches 97%.

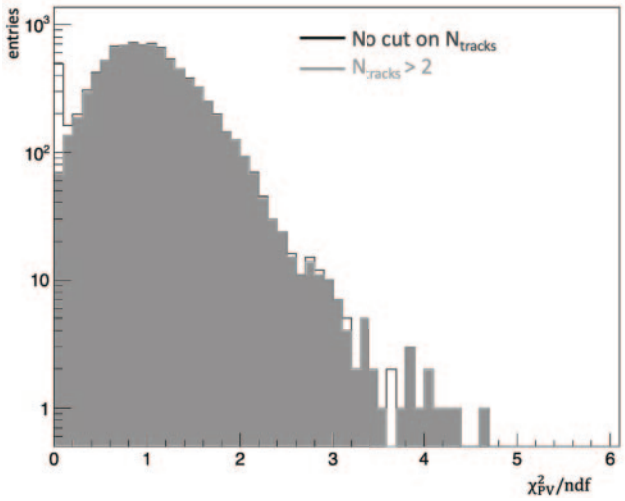

Fig. 7. – Reduced $\chi^2_{\rm PV}$ distribution. Black: total distribution. Grey: distribution requiring that the multiplicity of tracks associated to the primary vertex is bigger than 2.

Figure 8 shows the distributions of the residuals obtained from the difference between the fitted vertex coordinates and the coordinates from the MC truth. The resolutions (standard deviation of the residuals) are reported in table I for different selections of the multiplicity. They improve significantly for increasing multiplicity.

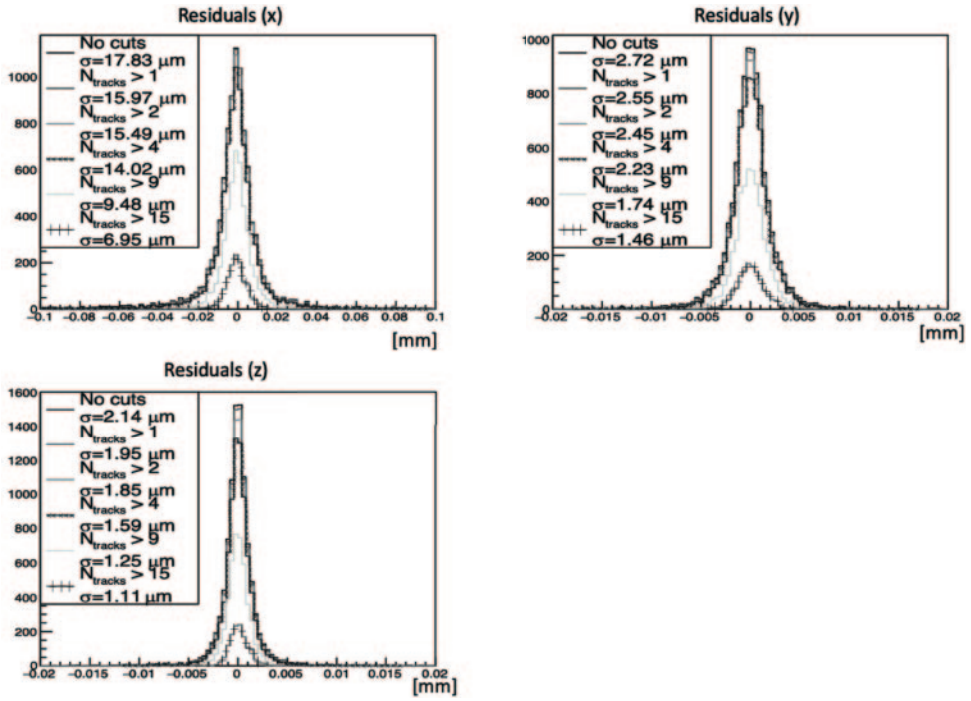

Fig. 8. – Residuals distributions obtained as the difference between the vertex x, y and z coordinates from the MC truth and the fitted primary vertex.

TABLE I. – *Resolution of the primary vertex coordinates for different selections of the track multiplicity associated to the primary vertex.*

Track multiplicity	σ_x [μm]	σ_y [μm]	σ_z [μm]
>2	16	2.5	2
>10	9	2	1
> 25	5	0.5	0.5

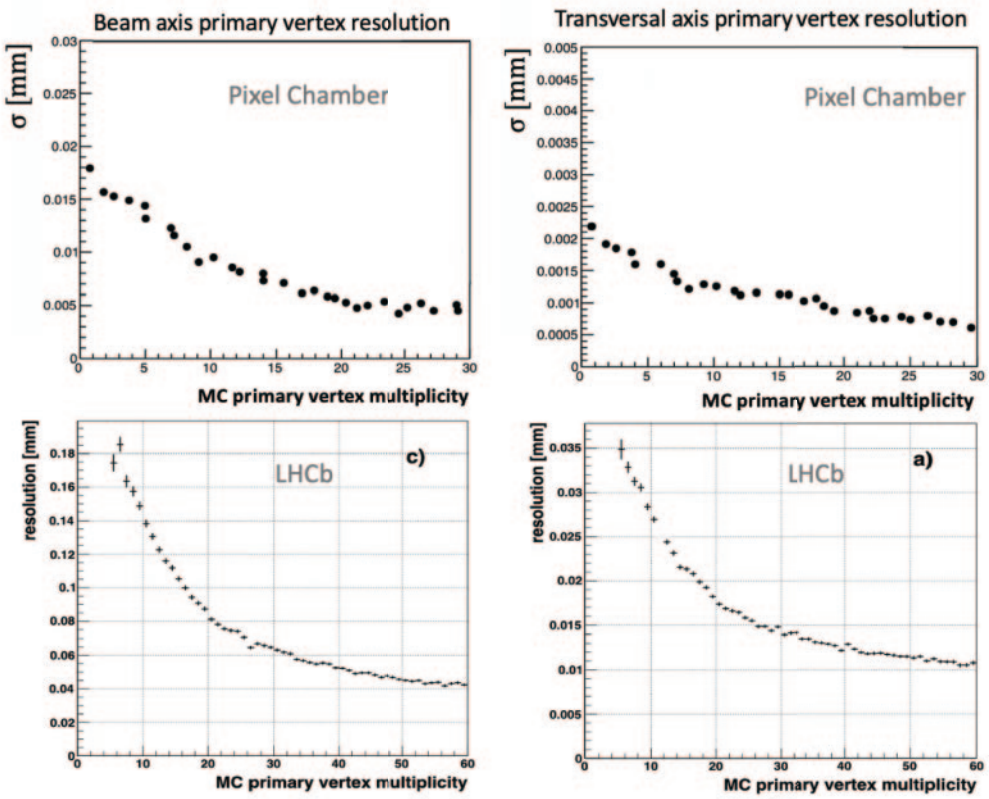

Fig. 9. – Primary vertex resolutions as a function of the number of tracks associated to the primary vertex reconstructed in Pixel Chamber (top) and LHCb (bottom) [14]: left panels show resolutions along the beam axes, right panels show resolutions along a transverse axis.

In fig. 9 the vertex coordinates resolutions *vs.* track multiplicity are shown and compared to LHCb [14]. Of course, the two experiments have very different setups and different beam energies, but it is interesting to observe that with Pixel Chamber it is possible to obtain resolutions that are about one order of magnitude better than those obtained with LHCb.

6. – Conclusions and outlook

In this paper we described briefly the idea of Pixel Chamber, a 3-dimensional active-target pixel matrix. According to simulations performed with Geant4, it is possible to obtain a high efficiency for the reconstruction of hadronic tracks and the primary interaction vertex inside the detector. The position of the primary vertex can be measured with very high precision.

Track reconstruction could be further improved taking into account multiple scattering. This will be done adding a Kalman filter fit to the algorithm. In addition, machine learning and neural networks might also be used to improve tracks and secondary vertices reconstructions.

At the moment, the algorithm for the reconstruction of secondary D^0 vertices is also under development and test. Preliminary results show that it is possible to reach very good resolutions for the secondary vertex reconstructions too. The obtained resolutions are ~ 30 μm, ~ 5 μm, ~ 4 μm along the x, y, z axes, respectively.

REFERENCES

[1] ALICE Collaboration, *J. Phys. G*, **41** (2014) 087001.
[2] ALICE Collaboration, *J. Phys. G*, **41** (2014) 087002.
[3] Bellini G. *et al.*, *Miniaturization of High-Energy Physics Detectors* (Springer) 1983, pp. 41–55.
[4] Usai G. *et al.*, *Pixel Chamber: A universal silicon heavy-flavor imager for fixed-target measurements of charm and beauty with unprecedented precision*, Project funded by the Sardinian Regional Government.
[5] Barnes V. E. *et al.*, *Phys. Rev. Lett.*, **12** (1964) 204.
[6] `https://geant4.web.cern.ch/`.
[7] Perrin-Terrin M., *Proceedings of the 24th International Workshop on Vertex Detectors (Vertex 2015)*, Vol. **254** (SISSA) 2015, p. 16.
[8] Apollinari G. *et al.* (Editors), *High-Luminosity Large Hadron Collider (HL-LHC) Technical Design Report V. 0.1*, CERN Yellow Reports: Monographs, Vol. **4** (CERN) 2017, pp. 1–516, CERN-2017-007-M.
[9] Aglieri Rinella Gianluca on behalf of the ALICE Collaboration, *Nucl. Instrum. Methods A*, **845** (2017) 583.
[10] Mangano M. L. *et al.*, *Nucl. Phys. B*, **373** (1992) 295.
[11] Alioli S., Nason P., Oleari C. and Re E., *JHEP*, **06** (2010) 043, arXiv:1002.2581.
[12] JaJa J., *Comput. Sci. Eng.*, **2** (2000) 43.
[13] Ester M. *et al.*, *Proceedings the Second International Conference on Knowledge Discovery and Data Mining (KDD-96)* (AAAI Press) 1996, pp. 226–231.
[14] Kucharczyk M., Morawski P. and Witek M., LHCb-PUB-2014-044.
[15] Agakichiev G., Barannikova O., Ceretto F., Faschingbauer U., Glässel P., Kolganova E., Ososkov G., Panebratsev Yu., Rak J., Saveljic N., Tserruya I., Ullrich Th. and Wurm J. P., *Nucl. Instrum. Methods*, **394** (1997) 225.